



# Spectroscopic diagnostics of an H $\alpha$ and EUV filament observed with THEMIS and SOHO

Brigitte Schmieder, Kostas Tziotziou, Petr Heinzel

## ► To cite this version:

Brigitte Schmieder, Kostas Tziotziou, Petr Heinzel. Spectroscopic diagnostics of an H $\alpha$  and EUV filament observed with THEMIS and SOHO. *Astronomy and Astrophysics - A&A*, 2003, 401, pp.361-375. 10.1051/0004-6361:20030126 . hal-03801649

**HAL Id: hal-03801649**

**<https://hal.science/hal-03801649>**

Submitted on 10 Oct 2022

**HAL** is a multi-disciplinary open access archive for the deposit and dissemination of scientific research documents, whether they are published or not. The documents may come from teaching and research institutions in France or abroad, or from public or private research centers.

L'archive ouverte pluridisciplinaire **HAL**, est destinée au dépôt et à la diffusion de documents scientifiques de niveau recherche, publiés ou non, émanant des établissements d'enseignement et de recherche français ou étrangers, des laboratoires publics ou privés.

# Spectroscopic diagnostics of an H $\alpha$ and EUV filament observed with THEMIS and SOHO

B. Schmieder<sup>1,2</sup>, K. Tziotziou<sup>1,\*</sup>, and P. Heinzel<sup>3</sup>

<sup>1</sup> Observatoire de Paris, Section de Meudon, LESIA, 92195 Meudon Principal Cedex, France  
e-mail: Brigitte.Schmieder@obspm.fr; Kostas.Tziotziou@obspm.fr

<sup>2</sup> Institute of Theoretical Astrophysics (ITA), University of Oslo, Blindern, 0315 Oslo, Norway

<sup>3</sup> Astronomical Institute, Academy of Sciences of the Czech Republic, 25165 Ondřejov, Czech Republic  
e-mail: pheinzl@asu.cas.cz

Received 27 February 2002 / Accepted 17 January 2003

**Abstract.** A long filament has been observed with *THEMIS/MSDP* and *SOHO/CDS - SUMER*, during a coordinated campaign (JOPs 131/95) on May 5, 2000. The data were (a) 2-D H $\alpha$  spectra, observed using *THEMIS*, (b) Lyman series spectra and Lyman continuum, observed using *SOHO/SUMER*, and (c) EUV spectra (in O v 629 Å, Mg x 624 Å, Si xii 520 Å, Ca x 557 Å and He i 584 Å) observed using *SOHO/CDS*. A large depression of the line emissions in *CDS* images represents the EUV filament. A computed model shows that the EUV filament consists of an extended in height cloud of low gas pressure at an altitude lower than the top of the H $\alpha$  filament, volume-blocking and absorbing coronal emission and absorbing transition region line emission. The optical thickness of the Lyman continuum is estimated by using the ratio of O v intensity inside and outside the EUV filament, while the optical thickness of H $\alpha$  is computed from the H $\alpha$  line profile by using an inversion technique. Using simultaneous H $\alpha$ , Lyman lines and Lyman continuum spectroscopic data, we performed detailed, non-LTE radiative transfer diagnostics of the filament plasma conditions. The optical thickness of the Lyman continuum is larger than that of the H $\alpha$  line by one to two orders of magnitude. This could be of a great importance for filament formation modeling, if we consider that more cool material exists in filament channels but is optically too thin to be visible in H $\alpha$  images.

**Key words.** Sun: filaments – line: profiles – radiative transfer – techniques: spectroscopic – methods: data analysis

## 1. Introduction

Filaments are commonly well observed on the disk in H $\alpha$ . They appear as dark long structures (called the “main body”) and lateral extensions named “barbs” or footpoints (Martin et al. 1998). They lie along longitudinal magnetic field inversion lines over weak field channels. The channels persist even if the filament has erupted. In H $\alpha$  intensity maps the areas corresponding to these channels are called “filament channels” and they are generally wider than the filament itself.

Dark filaments in EUV lines shortward of 912 Å (hereafter called “EUV filaments”) are frequently observed by the ultraviolet telescopes and spectrographs onboard the *SOHO* and *TRACE* satellites. They are associated with H $\alpha$  filaments, e.g. prominences seen against the disk, but their morphology is different to their H $\alpha$  counterparts. These dark EUV features have been already noticed by Schmahl & Orrall (1979) in data from ATM *Skylab* and from the *OSO 4* and *6* satellites. The lack of EUV line emission has been interpreted as due to an

absorption of the corresponding EUV lines, originating below the filament, by the hydrogen Lyman continuum. Thus, in places where these features are visible, one should expect a significant amount of neutral hydrogen, e.g. a cool prominence plasma with a temperature of the order of  $T \lesssim 10^4$  K.

Various kinds of EUV filaments have been recorded in many *SOHO/EIT* and *TRACE* images and movies and some of them have been associated with initial stages of coronal mass ejections (CMEs) related to an eruptive prominence (Plunkett et al. 2000). Recently, such large absorbing structures have been observed by *SOHO/CDS* in the Mg x line by Schmieder et al. (1998). Penn (2000), using *CDS* data and Mein et al. (2001), using *TRACE* data calculated the column hydrogen density for dark EUV filaments. In the case of prominences, Kucera et al. (1998) demonstrated that the dark regions observed in EUV coronal lines above the limb were due to the bound-free absorption in hydrogen and helium resonance continua. They also computed the hydrogen column density from absorption by the cool plasma and discussed the limits beyond which this continuum absorption is saturated. Chiuderi Drago et al. (2001), using *SOHO/CDS* and *SUMER* raster images to study the behaviour of EUV filaments, supported the Lyman-continuum absorption model by concluding

Send offprint requests to: B. Schmieder,  
e-mail: Brigitte.Schmieder@obspm.fr

\* Present address: National Observatory of Athens, Institute for Space Applications and Remote Sensing, 15236 Palea Penteli, Greece.

that while shortward of  $912 \text{ \AA}$  we typically see EUV filaments, longward of  $912 \text{ \AA}$  practically no signature of filaments is detected in transition-region lines.

Much wider EUV filaments compared to the  $H\alpha$  ones have been recently revealed by Heinzel et al. (2001) using *SOHO/CDS* and *THEMIS/MSDP* data. They demonstrated, by cloud model calculations as well as by an analytical derivation, that the ratio of the Lyman continuum to  $H\alpha$  opacity can reach a factor as high as 100. Thus the cool filament material is more abundant than  $H\alpha$  observations suggest, resulting in a wide observed EUV filament – due to the Lyman continuum absorption – even when the  $H\alpha$  contrast is already below the detection limit. Based on these results, Aulanier & Schmieder (2002) studied the magnetic nature of this wide EUV filament channel. They showed that the absorbing material condensations are present in magnetic dips, filled by cool material. In the lateral extensions of the EUV filament width, the dips are relatively low ( $>4000 \text{ km}$  above the photosphere) while in the main body of the filament, flux rope dips are filled by cool material up to  $1700 \text{ km}$ . As a consequence, the filament body mass can be larger than the  $H\alpha$  estimations.

In this paper we use the same coordinated observations of *THEMIS/MSDP* and *SOHO/CDS* - *SUMER* spectrographs to further study the large extension of the EUV filament compared to its  $H\alpha$  structure. Using the Coronal Diagnostic Spectrometer (CDS) raster images (Harrison et al. 1995), we confirm that the width of a clearly visible EUV filament largely exceeds the width of the corresponding  $H\alpha$  filament observed by *THEMIS*. We further develop the idea that this behaviour can be explained in terms of different opacities in the  $H\alpha$  line and in the Lyman continuum by using a non-LTE cloud model inversion (Mein et al. 1996; Heinzel et al. 1999) as well as an inversion method based on an extensive grid of non-LTE filament models previously computed by Molowny-Horas et al. (1999) and Tziotziou et al. (2001). Finally, the Solar Ultraviolet Measurements of Emitted Radiation spectrometer *SUMER* provided spectra of selected hydrogen Lyman lines and Lyman continuum; they are used, together with detailed non-LTE modeling, to better understand the physical conditions inside the EUV filaments.

The paper is organized as follows: the next section describes *THEMIS* and *SOHO* observations. In Sect. 3 we present a detailed analysis of *SOHO/CDS* EUV observations. We also perform an inversion of *MSDP*  $H\alpha$  line profiles in the filament to obtain 2D maps of the optical thickness in  $H\alpha$  and the Lyman continuum using two different methods and compare the results with non-LTE models based on *SUMER* spectra (Sect. 4). Finally, Sect. 5 contains the discussion and conclusions.

## 2. Observations

On May 5, 2000, a filament located at S 25 E 25-30 (at 08:00 UT) was the target of a joint *SOHO* and ground-based observatories (GBO) observational campaign. The campaign was coordinated at the *SOHO* MEDOC operation center (Orsay, France) and two different Joint Observing Programs were used successively, JOP131 and JOP95 (Schmieder et al. 2002).

### 2.1. THEMIS

The observations were performed with the Multichannel Subtractive Double Pass spectrograph *MSDP* (Mein 1991, 2002). The *MSDP* provides 9 simultaneous channels in the  $H\alpha$  line of a 2D area corresponding to the size of the wide entrance field-stop of the spectrograph, which is approximately  $150'' \times 25''$ . These 9 images correspond to positions in wavelength separated by  $0.24 \text{ \AA}$ . The wavelength range of each spectrum is  $0.08 \text{ \AA}$ . The data recorded on a CCD camera (with an exposure time of 100 ms and an acquisition time of 3.5 s) allow us to get a 3D data cube ( $x, y, \lambda$ ) of the region within 2.5 min. With the *MSDP* software we correct the data using the flat field and dark current registered at the disk center, then we get the  $H\alpha$  profile for each individual pixel of the entrance slit (pixel =  $0.2''$ ). Maps of intensities and Dopplershifts are derived by using the bisector technique (Fig. 1). According to this technique, the displacement of the middle of a chord with a given length  $2\Delta\lambda$  compared with the middle of the reference profile gives the Dopplershift value at  $\pm \Delta\lambda$ . The reference profiles are the mean profiles over the field-of-view, avoiding the brightest and darkest regions. During the observations the entrance field-stop was shifted 40 times within 3.5 min with a scan step of  $10''$ . By adding the elementary fields-of-view of the field-stop we can cover a wider region ( $\sim 150'' \times 400''$ ) in a spectral range of  $2.16 \text{ \AA}$ . The  $H\alpha$  filament region is shown in Fig. 1. We notice that the  $H\alpha$  filament is surrounded by a bright chromosphere.

### 2.2. SOHO/CDS

The two CDS JOPs were consecutively executed between 08:00-12:00 and 15:40-17:00 UT. During each of the CDS JOPs, two separate specific programs were run. In the first program we recorded 6 spectral lines in 50 min over a field-of-view of  $240'' \times 240''$ . In the second we recorded 14 spectral lines in 30 min with a field-of-view of  $120'' \times 240''$ . The spatial sampling for each spectral line was  $2'' \times 1.68''$ . The six spectral lines used in this study are: Si XII at  $520.60 \text{ \AA}$ , Ca X at  $557.77 \text{ \AA}$ , Ne VI at  $562.80 \text{ \AA}$ , He I at  $584.33 \text{ \AA}$ , Mg X at  $624.94 \text{ \AA}$  and O V at  $629.73 \text{ \AA}$ . The spectral dispersion is  $\sim 0.11 \text{ \AA}$  per pixel, 25 points are registered in each spectral window. The line profiles observed at pixels in the middle of the 08:30 UT raster are shown in Fig. 3. The ratio of the line-center intensities between filament and quiet Sun is 0.33 (0.8) for Si XII, 0.16 (0.1) for He I, 0.14 (0.16) for Mg X and 0.1 (0.05) for Ca X (the values in parentheses are derived from averaged profiles observed at 15:30 UT). Thus the contrast of the EUV filament is lower for Si XII than for the other lines. In Fig. 4 we present an overlay of the  $H\alpha$  filament onto the CDS images. There is a decrease of intensity at the location of the filament compared to the quiet Sun.

### 2.3. SOHO/SUMER

The *SUMER* spectrometer on-board the *SOHO* spacecraft is described in Wilhelm et al. (1995). The slit of *SUMER* ( $1'' \times 120''$ ) was oriented north-south and was centered in the middle of CDS rasters (see Fig. 2). The spectral lines of the Lyman

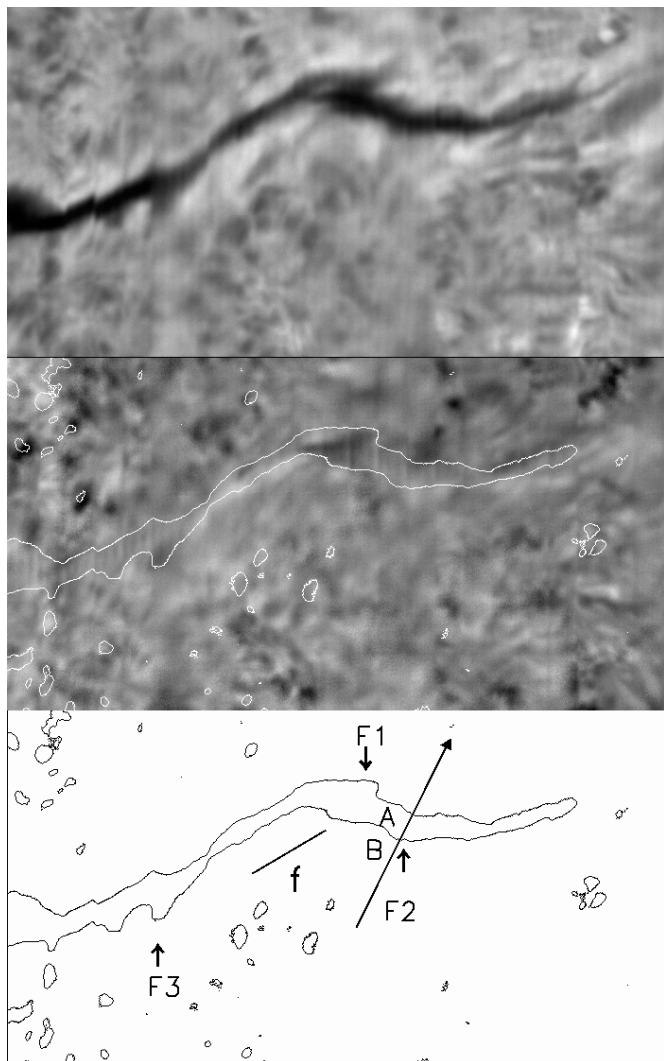


**Fig. 1.** Filament of May 5, 2000 in  $H\alpha$  observed by *THEMIS/MSDP* ( $280'' \times 150''$ ): top panel is the intensity map ( $I$  at  $\pm 0.256 \text{ \AA}$ ), the middle panel is the Dopplershift map ( $V$  at  $\pm 0.256 \text{ \AA}$  between  $\pm 2 \text{ km s}^{-1}$ ) overlaid by an intensity contour. Downflows (dark regions) are observed near the footpoints of the filament (F1, F2, F3). The bottom panel represents a sketch with different letters used in the text. A chromospheric fibril is represented by a straight line,  $f$ . The long inclined arrow represents the *SUMER* slit position and indicates the North direction. Position A corresponds to the filament main body, position B to the filament channel nearby.

series of hydrogen from L2 to the Lyman continuum (e.g.  $L\beta$ ,  $L\gamma$ ,  $L\delta$ ,  $L5$ ,  $Lc$ ) were observed during the entire *CDS* observation period. The spectral dispersion is  $0.0445 \text{ \AA}$  per pixel. To be able to observe from  $L\beta$  to the Lyman continuum we selected three wavelength windows centered around 924, 955 and  $1010 \text{ \AA}$ , respectively. This means that the spectra are recorded sequentially. Full spectra of approximately  $45 \text{ \AA}$  are recorded with an exposure time of 120 s followed by sequences of partial spectra (centered on the wavelengths of interest) with a 28 s exposure time. *SUMER* has two detectors (named A and B), however in our observing programme only the detector A was used. Over the central part of the detectors an opaque KBr photocathode material is deposited that

increases the quantum detection efficiency. The strong intensity lines are registered on the bare parts of the detector in order to spare the detector. We also observed other transition-region lines: the C III triplet at  $977.7 \text{ \AA}$ , O VI at  $1031.9 \text{ \AA}$ , S VI at  $933.4$ ,  $944.5$  and  $991.8 \text{ \AA}$  and several photospheric lines that are used for the wavelength calibration (O I and N I).

During data reduction, we destreched the spectra using the *SOHO* software, corrected them by using the flat field observed on the same day and calibrated the wavelengths with the software developed at the Institute of Theoretical Astrophysics (ITA). The intensity calibration was performed with the radiometry procedure of Wilhelm et al. (1997). The absolute radiometric calibration is now accurate to within 30–40% (Schüle et al. 2000).

## 2.4. $H\alpha$ and EUV filament widths

Figure 1 shows that the  $H\alpha$  filament consists of a main body and several footpoints (e.g. F1, F2, F3). All along the filament, on both sides, we observe some enhancements of brightness which may correspond to weak parasitic polarities (Aulanier & Schmieder 2002). In the filament channel we observe some chromospheric fibrils parallel to the filament axis (e.g. see the fibril  $f$  in Fig. 1). The width of the  $H\alpha$  filament body is between  $10''$  and  $20''$ , with some gaps, where the filament is not visible (e.g. between positions F3 and F1).

The EUV filament, which is observed with *CDS* and is associated with the  $H\alpha$  filament, is wide compared to the  $H\alpha$  filament (see Figs. 2 and 4). It consists of a complex pattern of dark regions, less and less homogeneous as one moves away from the main filament axis. The EUV filament consists of two sections separated by some brightening (Fig. 2). The left section overlays the  $H\alpha$  filament and the dark chromospheric fibril  $f$ . The right section shows a triangle shape corresponding to a EUV lateral extension towards the south. A quantitative comparison of the width of the filament in  $H\alpha$  and EUV is well illustrated in Fig. 7. The EUV width ( $\sim 30''$ ) is twice as large as the  $H\alpha$  filament in some locations, particularly when the filament is between bright areas (faculae regions). In other locations the EUV width (around  $100''$ ) is about five times larger than the  $H\alpha$  width, where an EUV lateral foot does exist.

During the first observing sequence (08:00–12:00 UT), the *SUMER* slit was positioned to cross the filament at a location A, labeled in Fig. 1. At this location, the  $H\alpha$  filament is narrow ( $10''$ ) and the EUV filament has a lateral extension. We observe that the Lyman lines profiles are reversed at the location of the main body of the filament (e.g.  $L\beta$  and  $L\epsilon$  lines in Fig. 5 and Lyman profiles in Fig. 17). They are not reversed (but have a low intensity) above the EUV lateral extension corresponding to location B in Fig. 1. According to previous investigations, Schmieder et al. (1998) showed that higher Lyman lines are reversed in the positions of the filament and unreversed in the quiet Sun. In Fig. 5 we notice that the extension of the reversal of  $L\beta$  line is as large as the width of the  $H\alpha$  filament.

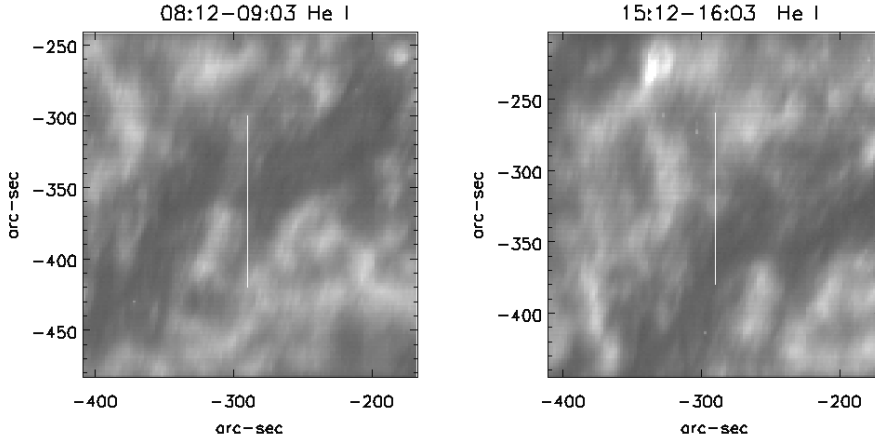


**Fig. 2.** CDS He I images overlaid by the SUMER slit according to the recorded positions.

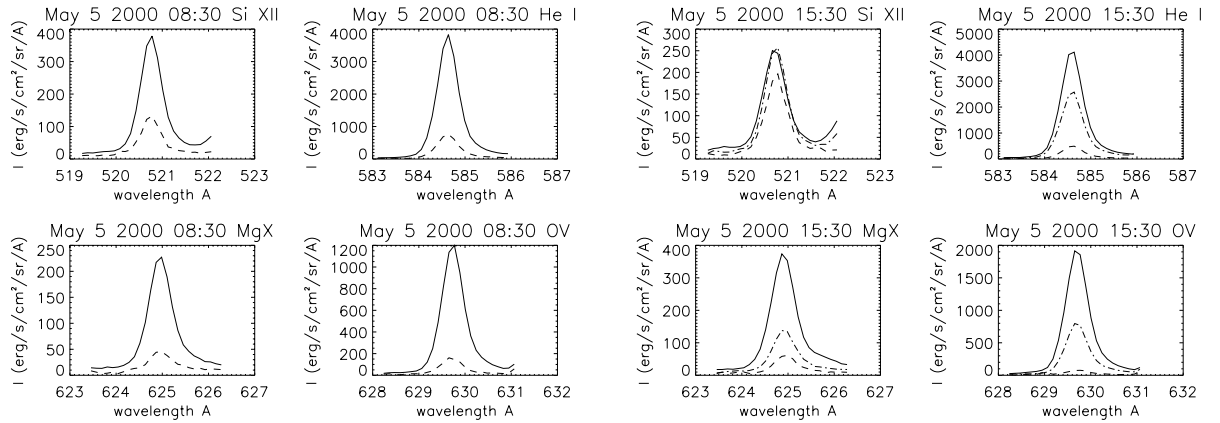


**Fig. 3.** Profiles of CDS lines at 08:30 UT and at 15:30 UT (full line: quiet Sun averaged over 40'', dashed-dotted: lateral extensions averaged over 20'', dashed line: EUV filament averaged over 20'').

### 3. Filament absorption and volume-blocking

In a previous paper (Heinzel et al. 2001) we have studied the filament absorption in  $H\alpha$  and EUV by means of two different simplified methods, using *THEMIS* and *CDS* data, respectively. Below we discuss the results obtained from a more detailed analysis of *SOHO/CDS* EUV observations and compare them with results of  $H\alpha$  data inversions.

#### 3.1. Lyman continuum opacity derived from CDS observations

Reduced emission in coronal and transition-region (TR) lines is typically observed on CDS rasters (Fig. 4). The proper interpretation of this reduced emission strongly depends on the formation heights of the lines used and on the actual heights of the EUV filament that can either absorb the radiation of a EUV line or simply block a certain volume in the corona so that the coronal line formed at a given temperature cannot be emitted there. As already discussed in Heinzel et al. (2001), one has to distinguish between two categories of EUV lines as observed by CDS. These are *TR lines* formed at lower temperatures and within the solar transition region (like the O v line) and *coronal lines* formed at temperatures around or higher than  $10^6$  K, like Mg x and Si xii. Below we discuss how the extended EUV filament affects the emission in such lines. In general, we

will consider two effects: EUV line absorption by the hydrogen Lyman continuum and EUV line blocking by the volume of the filament.

##### 3.1.1. Transition-region (TR) lines

We assume that the brightness depression observed in the O v transition-region line is entirely due to absorption by Lyman continuum. The Lyman-continuum optical thickness at the wavelength of a EUV line is given by

$$\tau_{\lambda}(i, j) = -\ln \left[ \frac{I(i, j) - I_{fg}}{I_{bg}} \right] \quad (1)$$

where  $I(i, j)$  is the intensity of the EUV line at the raster pixel  $(i, j)$ ,  $I_{bg}$  the intensity of the background under the filament (taken to be the quiet-Sun intensity  $I_{QS}$  for O v) and  $I_{fg}$  is the intensity of the foreground, here assumed to originate in the prominence-corona transition region (PCTR). All intensities in Eq. (1) are the integrated intensities because  $\tau_{\lambda}$  does not depend on the wavelength within the line profile. We use the notation of  $I_{QS}$  for the averaged intensity outside the EUV filament, but this needs not necessarily be the actual quiet-Sun value. Note that the computation of the optical thickness does not require the absolute intensity calibration since we use only the line ratios.

Figure 8 shows a two-dimensional plot of the Lyman-continuum optical thickness  $\tau$  at the wavelength corresponding



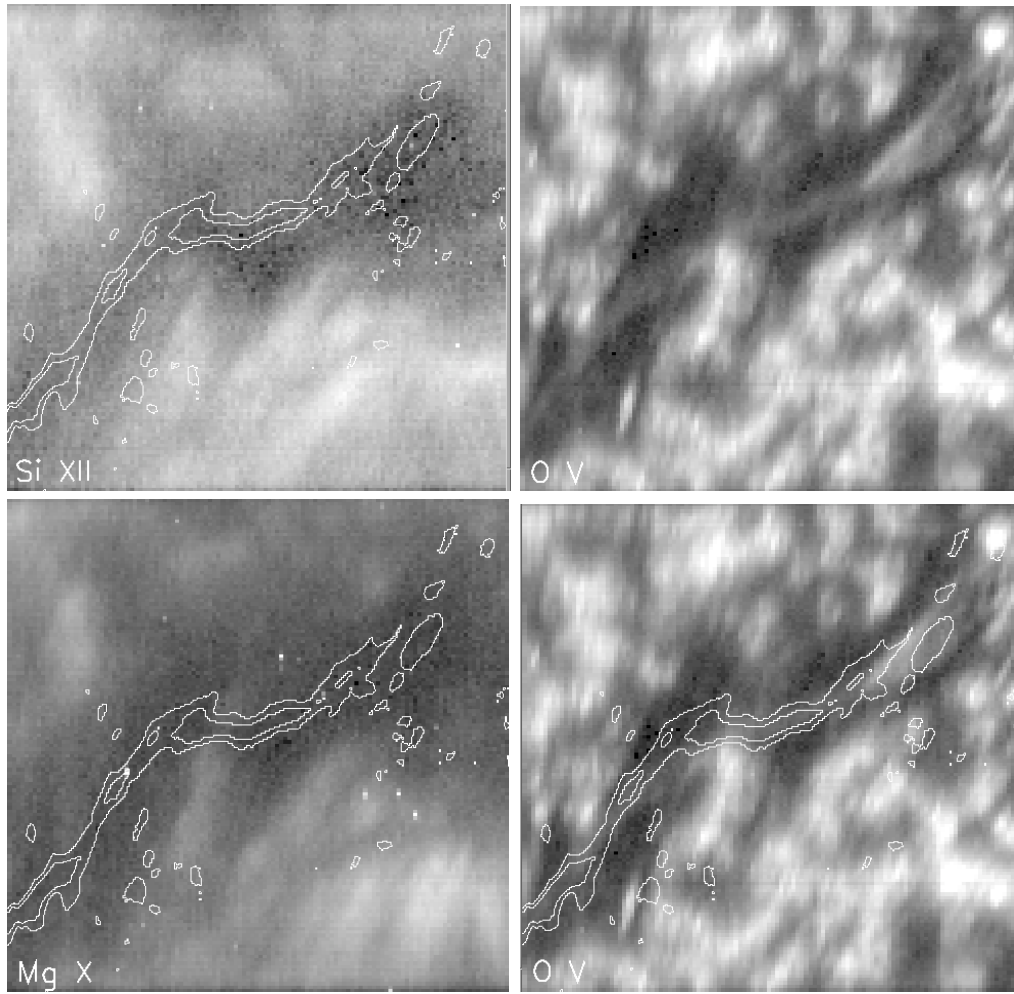


**Fig. 4.** CDS images overlaid by *THEMIS* filament contours. The contours correspond to the  $H\alpha$  contrast ( $C_{H\alpha} = -0.2, -0.3, \tau(H\alpha) \sim 1$  for  $C_{H\alpha} = -0.3$ , see Heinzel et al. 2001 for definition). There is a decrease of intensity of CDS lines at the location of the filament compared to the quiet Sun. The width of the EUV filament is large, between  $50''$  and  $100''$  in all the CDS rasters (see Sect. 2.4 and Fig. 7). The  $H\alpha$  filament width is only  $10''$ – $20''$ . Notice the bright spine at the location of the  $H\alpha$  filament in the O v image.

to the O v line ( $629.73 \text{ \AA}$ ). We overlay there a contour of the  $H\alpha$  filament ( $C = -0.2$ ) and the contour of  $\tau(629) = 1$ . These contours delineate approximately what we call the EUV filament extension. In central parts of the  $H\alpha$  filament,  $\tau(629)$  is not correctly computed because the background emission is fully absorbed. At these points we measure  $I_{fg}$ , the emission of the transition region on the top of the filament (see the spine in Fig. 4). In the EUV filament we neglect this emission ( $I_{fg} = 0$ , see Table 1).

Because various observed EUV lines are located at different wavelength positions in the range of hydrogen Lyman continuum, it is useful to speak about Lyman continuum absorption in terms of the opacity at the *continuum head* at  $912 \text{ \AA}$ . To convert  $\tau$  determined at the position of a EUV line to that at  $912 \text{ \AA}$ , we use the well-known  $\lambda^3$ -dependence for hydrogen continua opacity (e.g. Mihalas 1978) and get factors 0.320 for Mg x and O v, 0.229 for Ca x and 0.186 for Si xii.

In Table 1 we present characteristic values of line intensities (for O v, Si xii and Mg x) averaged along the vertical central cut of the CDS raster ( $x = 60$  in Fig. 7) which corresponds to the position of the *SUMER* slit. Variations of  $\tau(912)$

along this cut are drawn in Fig. 9. This cut has been chosen for a direct comparison with *SUMER* results (see Sect. 4). The value of  $\tau(912)$  increases in the filament channel from zero to about 10 as we reach the boundary of the  $H\alpha$  filament. Using data in Table 1, one gets from the O v line (with Eq. (1)) a mean representative value  $\tau(912) \sim 5.3$ . This is consistent with the value obtained from the Mg x line, provided that we assume  $I_{bg} = I_{QS}$  as we did in Heinzel et al. (2001) (see discussion below).

For this transition-region line, the uncertainty in determination of  $\tau$  is, however, relatively large compared to coronal lines. This is due to the fact that TR lines reveal much stronger variations of the background intensity. In the case of O v we can see in Fig. 7 variations between 500–1000 cgs units which, using Eq. (1) and the data in Table 1, give variations in  $\tau(912)$  between 4.2–6.3.

### 3.1.2. Coronal lines

The situation with coronal lines is much more complicated. There are three possibilities for the interpretation of

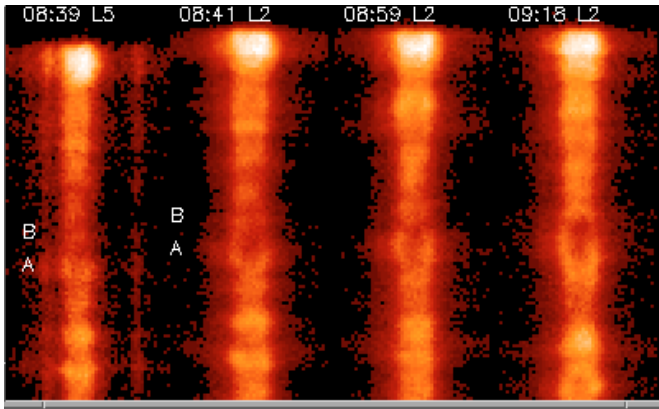


**Fig. 5.** *SUMER* spectra along the 120'' long slit (vertical direction). The dispersion of the spectra is in the horizontal direction. The left spectrum is  $\text{L}\epsilon$  (named L5) and the 3 others are  $\text{L}\beta$  (named L2). The time of the observations is indicated at the top of the spectra. The first two are close in time. The other two show time evolution. The filament corresponds to locations where the lines are reversed (indicated by the letter A); the nearby channel corresponds to locations with reduced intensities (indicated by the letter B). North is down.

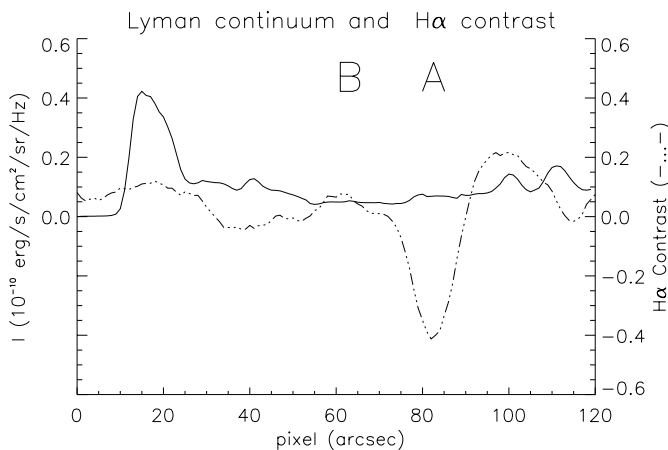


**Fig. 6.** Lyman continuum intensity along the *SUMER* slit (solid line) on May 5, 2000 at 08:39 UT. The EUV filament corresponds to pixels 40 to 100 with a nearly constant and low intensity (region B). For the first 10 pixels the values are not real. The intensity bump between pixel 10 to 30 represents a small part of the quiet Sun. The  $\text{H}\alpha$  contrast is drawn as dashed-dotted line. The  $\text{H}\alpha$  filament (region A) corresponds to pixels 75 to 90 with a contrast lower than  $-0.1$ .

the brightness depression in coronal lines: (i) by presence of a void around the whole filament structure ( $\text{H}\alpha$  and EUV), i.e. the missing hot plasma, (ii) the filament or any cool material is located relatively high in the corona compared to the scale-height of the coronal line emission so that a large fraction of coronal radiation emitted below the filament can be absorbed by the Lyman continuum, and (iii) the filament is rather extended in height. The presence of the cool filament (both  $\text{H}\alpha$  and EUV) blocks the coronal volume which would otherwise emit in coronal lines. The absorption in that case could be negligible because the Lyman continuum optical thickness can be very small.

Of course, the combination of these three effects can occur. In order to explain quantitatively the  $\text{Mg x}$  and  $\text{Si xii}$  measurements, we have constructed a model which takes fully into account all these mechanisms. The situation can be simplified by assuming that even if there is a void, this void (or coronal cavity) is much more extended than the EUV filament. Under this condition, the so-called “quiet-Sun” intensity  $I_{\text{QS}}$  is just the mean intensity in the raster outside the EUV filament and represents the intensity of the corona surrounding the filament. The non-existence of a void is an assumption but seems to be justified by the fact that the EUV filament has the same pattern in the transition-region line (e.g.  $\text{O v}$ ) and in the coronal lines ( $\text{Mg x}$  and  $\text{Si xii}$ ).

The model that we have constructed takes into account the Lyman-continuum absorption and the volume-blocking and gives consistent results for both  $\text{Mg x}$  and  $\text{Si xii}$  lines. Having such a model, we can compute the optical thickness in these two lines and they must be the same as that derived from the  $\text{O v}$  line. However, this is difficult to achieve because we do not know the heights of the bottom and top parts of the EUV filament and, moreover, we should take into account the height variations of the coronal line emissivity. To avoid these difficulties, Heinzel et al. (2001) used in their exploratory paper a crude approximation that  $I_{\text{bg}} = I_{\text{QS}}$ . Here we will use the results of a much more complex modelling approach that is presented in Heinzel et al. (2003). The basic idea is to use  $\tau_{912}$  derived from TR line analysis ( $\text{O v}$  in our case) and compute the absorption and volume-blocking consistently in two coronal lines,  $\text{Mg x}$  and  $\text{Si xii}$ , which have different scale-heights. For each line we use Eq. (1), where now  $I_{\text{fg}} = [1 - f(h'')]I_{\text{QS}}$  and  $I_{\text{bg}} = f(h')I_{\text{QS}}$ . The function  $f(h)$  describes the variation of the coronal emissivity with height and has an approximate form  $f(h) = 1 - \exp(-h/H)$ , where  $h$  is the height in the corona and  $H$  is the scale-height of the coronal emission. From Eq. (1), applied to the two lines, it is possible to obtain two heights  $h'$  (bottom of EUV filament) and  $h''$  (top of EUV filament), by using an iterative method (for details see Heinzel et al. 2003). The scale-height  $H$  for each line can be obtained from quiet-Sun coronal observations of Fludra et al. (1999) (see their Fig. 2), by using the Abel transform.

Applying this procedure to our CDS data, we have arrived at the following conclusions. The data cannot be interpreted in terms of quiet-Sun scale-heights for  $\text{Mg x}$  and  $\text{Si xii}$ ; no solution is obtained from the iterative method. This is because our filament is located in an active region (see Aulanier & Schmieder 2002). In fact our calibrated intensities are much higher compared to quiet-Sun intensities reported in Brooks et al. (1999). According to W. Thompson (private communication),  $\text{Si xii}$  shows a strong increase with the solar cycle and our observations were done during the solar maximum.

In this case one can use the results of Sterling et al. (1999) that show that in the active region, the  $\text{Mg ix}$  scale-height is similar to that for the quiet-Sun derived from Fludra et al. (1999), but hotter line emission is much more concentrated towards the limb. Assuming similar behaviour also for  $\text{Mg x}$ , we took in our analysis  $H$  for  $\text{Mg x}$  from Fludra et al. (1999) (about 30 000 km) and using  $f(h)$  we computed the height at which  $I_{\text{fg}}$  becomes equal to the value of  $I_{\text{fg}}$  measured in

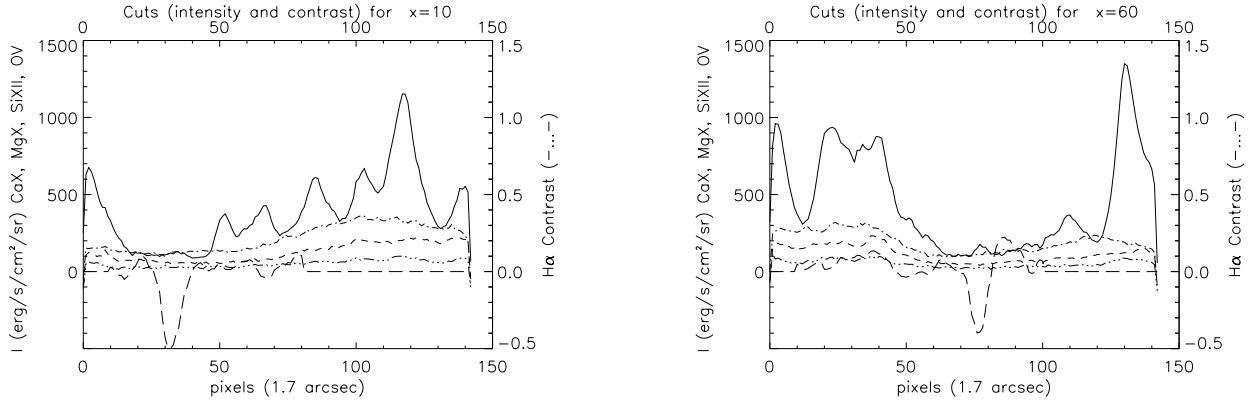


**Fig. 7.** Cuts of integrated intensities of CDS lines at different positions in the rasters ( $x = 60$  corresponds to the center cut in the raster, which is the position of the *SUMER* slit) observed between 08:12 and 09:03 UT in O v (solid line), Si xii (dashed-dotted line), Mg x (dashed line), Ca x (dashed-dot-dot-dot line). Cuts in the 2D contrast H $\alpha$  image are drawn as well. The dips of the curves show the low emission/absorption, in the EUV/H $\alpha$  filament.

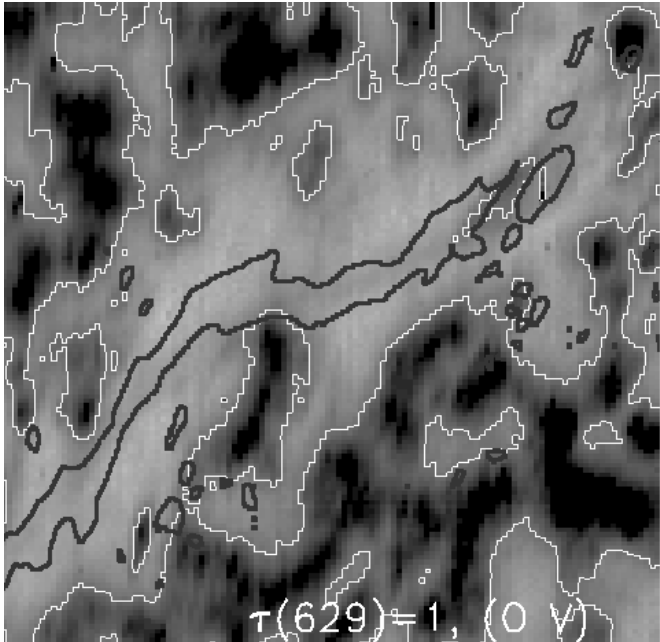


**Fig. 8.** Map ( $240'' \times 240''$ ) of  $\tau$  of Lyman continuum at  $629 \text{ \AA}$  overlaid by the H $\alpha$  contour. The black contour corresponds to a contrast  $C_{H\alpha} = -0.2$  and the white contours of  $\tau(629) = 1$  derived from O v CDS observations. The grey scale of the Lyman continuum optical thickness at  $629 \text{ \AA}$  varies from 0 to 3.2.

the MgX raster. This corresponds to the height of the top of the H $\alpha$  filament (about 45 000 km). Then using this filament height and  $I_{fg}$  for Si xii, we computed the scale-height  $H$  for this line. It is considerably reduced compared to the quiet-Sun one (about 42 000 km compared to 85 000 km), which is consistent with the findings of Sterling et al. (1999). Now using this new  $H$  for Si xii, we were able to obtain a plausible solution for heights  $h'$  and  $h''$  within the EUV filament extension. For  $\tau(912) = 5.6$ , as obtained above from typical O v line data,  $h'$  is about 27 000 km and  $h''$  about 37 000 km. The heights are generally lower for larger  $\tau$  and the difference  $h'' - h'$  (i.e. the geometrical thickness of the EUV structure) also decreases

**Table 1.** Integrated intensities for transition region and coronal lines in units of  $\text{ergs s}^{-1} \text{cm}^{-2} \text{sr}^{-1}$ , where  $f$  is a function of height (see text).

line	$I_{fil}$	$I_{QS}$	$I_{fg}$	$I_{bg}$	$\tau_{912}$
Si xii	120	260	90	$f \times 260$	
Mg x	70	180	40	$f \times 180$	
O v	150	1000	0	1000	6.3
	150	500	0	500	4.2

at higher  $\tau$  values. The Ca x intensities are consistent with the present model.

A comment should be made on the height of the H $\alpha$  filament which was seen on the limb a few days prior to our observations. According to our estimates, this height did not exceed 20 000 km. From our models we get some 45 000 km. However, this high value could be explained by two facts: first, above the dense H $\alpha$  filament we have similar hotter and rare plasma as detected in the EUV channel which blocks the coronal radiation – this layer is practically transparent in H $\alpha$  (see Heinzel et al. 2003) and thus cannot be seen on the limb and also does not affect the analysis in Sects. 3.3 and 4. It is also quite possible that the true height derived from limb observations would be larger if one would use high-quality coronagraphic observations with appropriately long exposures.

These heights justify our previous results (Heinzel et al. 2001), at least for Mg x, because  $h'$  is comparable to the Mg x scale-height. Finally, these structures extended in height must have temperatures and gas pressures (densities) which will give us relatively small  $\tau(912)$ , between zero and say 10 (see Fig. 9). Heinzel et al. (2003) discuss this in detail and show that temperatures  $T$  of the order of 12 000 K and gas pressures around  $10^{-2} \text{ dyn cm}^{-2}$  satisfy this condition. Decreasing  $T$  or increasing the pressure would require that a rather small geometrical filling factor is assumed.

The model derived in this section shows a consistent view of EUV large filament: an extended in height cloud of low gas pressure at an altitude lower than the top of the H $\alpha$  filament absorbing and blocking coronal emission and absorbing transition region line emission. We have computed possible altitudes of



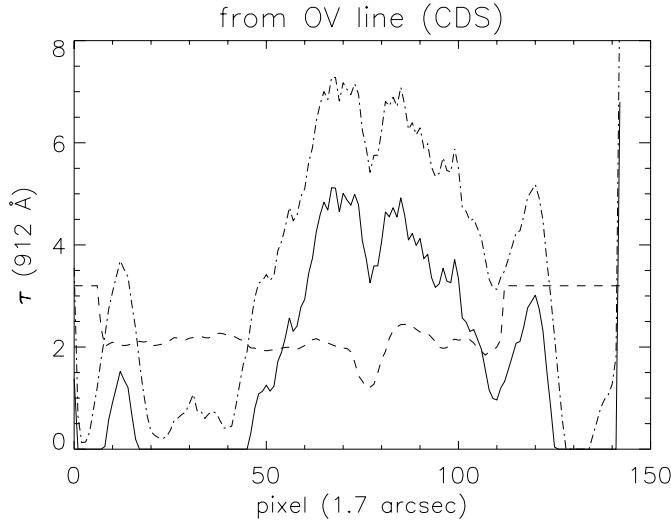


**Fig. 9.** From CDS observations (Ov line), computation of  $\tau(912 \text{ Å})$  for two different background values ( $I_{bg} = 500$ , solid line,  $I_{bg} = 1000$ , dotted dashed line). A cut of  $H\alpha$  intensity is drawn in order to show the position of the  $H\alpha$  filament (at pixels 70–80) in an arbitrary unit (dashed line).

the EUV structure but we have to keep in mind that uncertainties still do exist, particularly the scale-heights of coronal lines in the active corona. New studies, similar to those of Fludra et al. (1999) for 1996 observations should be performed in the corona during the maximum of solar activity. The sensitivity of different ions to an increase in temperature is quite different (Fludra et al. 2002).

### 3.2. Non-LTE $H\alpha$ cloud model inversion with constant source function

#### 3.2.1. The method

For this inversion method we consider the cloud model with a constant source function, described in Mein et al. (1996) and Heinzel et al. (1999). It is an iterative method.

The background intensity has been calculated from the average intensity of a small region close to the filament. This background intensity is almost equal to that of the quiet Sun. For the calibration of all intensities (background and observed profiles) relative to the quiet-Sun continuum we have used a proportionality factor (Molowny-Horas et al. 1999; Tziotziou et al. 2001) which is calculated by comparing the observed background with the quiet Sun profile of David (1961).

At each iteration step we calculate a synthetic profile  $P'$  and the iteration is stopped when the intensity difference (in all considered profile wavelengths) between two successive synthetic profiles is less than  $10^{-9}$ . The convergence is usually obtained after a few tens of iterations. If the convergence condition is not satisfied after 500 iterations, it is assumed that there is no solution. The difference between the observed profile  $P$  and the converged profile  $P'$  is also calculated. This inversion method returns the values for line-center optical thickness  $\tau_{max}$ , velocity  $V$ , Doppler width  $\Delta\lambda_D$  and source function  $S$  that best describe an observed profile.

#### 3.2.2. Results

We consider only points within the filament that have a contrast profile less than 0.96 ( $C_{H\alpha} < -0.04$ ). We thus exclude the borders where the filament is extremely optically thin and we may be observing (part of) the chromospheric background. We also consider only solutions with a difference lower than 0.005 between the observed and the converged synthetic profile, assuming thus a margin of error in observed intensities less than 0.5%.

In Fig. 10 we present the distributions of velocity  $V$ ,  $H\alpha$  line-center optical thickness  $\tau_0$ , Doppler width  $\Delta\lambda_D$  and source function  $S$  derived from this inversion method. These distributions have an average velocity of  $0.6 \text{ km s}^{-1}$ , an average optical thickness of 0.66, an average Doppler width of  $0.44 \text{ Å}$  and an average source function of 0.055 relative to the continuum. The Doppler width distribution shows two peaks at 0.4 and  $0.48 \text{ Å}$ . The latter corresponds – as its spatial distribution within the filament reveals – to regions with a local background that is brighter than the one used for the inversion. Comparing an observed profile to a darker background increases the Doppler width and hence this explains the inversion results which give higher Doppler widths for these regions of the filament. As it is known, the line-center optical thickness  $\tau_0$  decreases when the Doppler width  $\Delta\lambda_D$  increases. Since the calculated mean Doppler width from the inversion seems to be higher than the one expected from the literature for a typical filament, it means that the calculated line-center optical thickness represents a lower limit.

The optical thickness defined as

$$\tau_\lambda = \tau_0 \times \exp \left[ - \left( \frac{\lambda - \lambda_0 - \lambda_0 \frac{V}{c}}{\Delta\lambda_D} \right)^2 \right] \quad (2)$$

where  $\lambda_0$  is the  $H\alpha$  line-center wavelength and  $c$  is the speed of light, depends on two of the inversion parameters, the velocity  $V$  and the Doppler width  $\Delta\lambda_D$ . The overestimation of the Doppler width in a few regions within the filament results there, as the above equation indicates, in an underestimation of the actual amplitude of the velocity. We should also point out that a direct precise calculation of both temperature and microturbulence for  $H\alpha$  with an inversion method, instead of the Doppler width, is not accurate due to the nature of the line which is dominated by photoionization and not by collisions (Tziotziou et al. 2001). In Fig. 11 we show a scatter plot between the calculated source function and the optical thickness. As Mein et al. (1985) have shown, the determination of the source function with a cloud model for small optical depths is not accurate. For higher line-center optical thicknesses, which obviously represent the denser central parts of the filament, the scatter plot suggests a mean source function around 0.06 relative to the continuum which is close to the approximate value of 0.08 that Mein et al. (1996) obtained. This means that the incident radiation, which comes from a large area of the solar surface and defines the radiation field within the filament and hence the source function, is almost that of the quiet Sun.

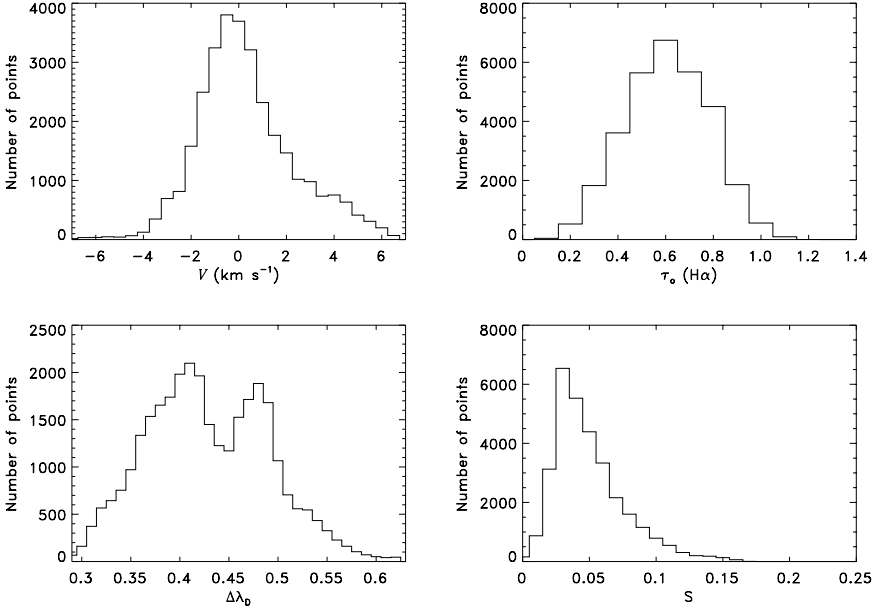


**Fig. 10.** Histograms of velocity  $V$ ,  $H\alpha$  optical thickness  $\tau_0$ , Doppler width  $\Delta\lambda_D$  and source function  $S$  in the  $H\alpha$  filament for the inversion method with constant source function described in Sect. 3.2.

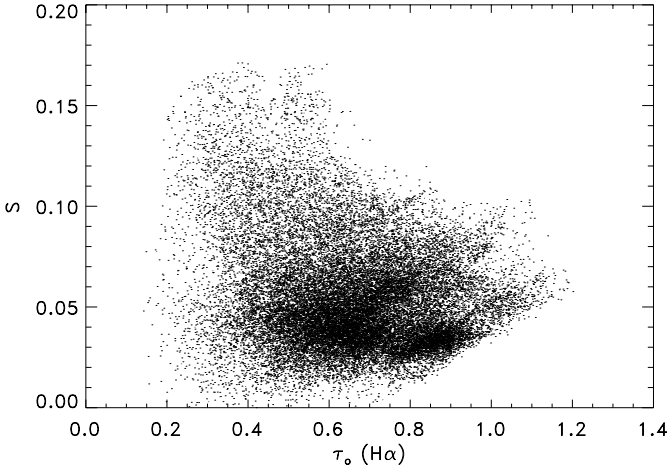


**Fig. 11.** Scatter plot between the calculated source function  $S$  and the optical thickness  $\tau_0$  for the inversion method with constant source function relative to the continuum described in Sect. 3.2.

### 3.3. Non-LTE $H\alpha$ grid cloud model inversion

We will consider now another inversion method based on non-LTE calculations for which the source function is not constant but varies as a function of line-center optical depth.

#### 3.3.1. The grid

For this inversion method we have constructed a large grid of models with a multi-level non-LTE transfer code which calculates the  $H\alpha$  line formation inside an isolated cloud lying above the solar surface. We used a five level plus continuum hydrogen model atom (see also Sect. 4). For details of all calculations described in this section we refer the reader to Molowny-Horas et al. (1999) and Tziotziou et al. (2001). The grid of hydrogen models depends on five free parameters: kinetic temperature ( $T$ ), electron density ( $N_e$ ), microturbulence ( $\xi_t$ ), cloud velocity ( $V$ ) and geometrical thickness ( $Z$ ). The range of values

**Table 2.** Parameters used for the calculation of the grid of models. The total number of the computed models is 81160. We only compute for positive velocities (the non-LTE results are identical for negative and positive velocities).

Parameter	Range	Step
$V$ (km s <sup>-1</sup> )	-5–5	2.5
$T$ (K)	6000–11 000	500
$Z$ (km)	1000–5000	500
$\xi_t$ (km s <sup>-1</sup> )	3–10	1
$N_e$ (cm <sup>-3</sup> )	$5 \times 10^9$ – $4.9 \times 10^{10}$	$2 \times 10^9$
	$5.3 \times 10^{10}$ – $6.5 \times 10^{10}$	$4 \times 10^9$
	$7.5 \times 10^{10}$ – $2.15 \times 10^{11}$	$2 \times 10^{10}$
$H$ (km)	20 000	–

for these parameters is given in Table 2 where  $H$  is the height of the structure above the solar surface. The results of calculations are the hydrogen level populations as a function of line-center optical depth. They are used for the calculation of the source function  $S$ .

For the incident radiation on the filament, which as we have already mentioned strongly drives the radiation field within the filament and affects the calculation of the source function, we have used the quiet-Sun incident radiation from David (1961). This is quite justified as the results of Sect. 3.2.2 have indicated. The same quiet Sun incident radiation was used for the transmitted (partially absorbed) radiation of the optically thin part of the filament. By solving the radiation transfer equation for the cloud, the  $H\alpha$  profiles are finally calculated. A grid-based inversion procedure is afterwards implemented, where we compare the observed spectral line profiles with each of the grid model profiles and find the best match between the two by a  $\chi^2$ -minimizing procedure. This inversion procedure gives the corresponding values of our free parameters ( $N_e$  and  $Z$  are combined into one parameter, the emission measure  $Q$  defined as  $N_e^2 Z$ ), as well as the  $H\alpha$  line-center optical thickness at each

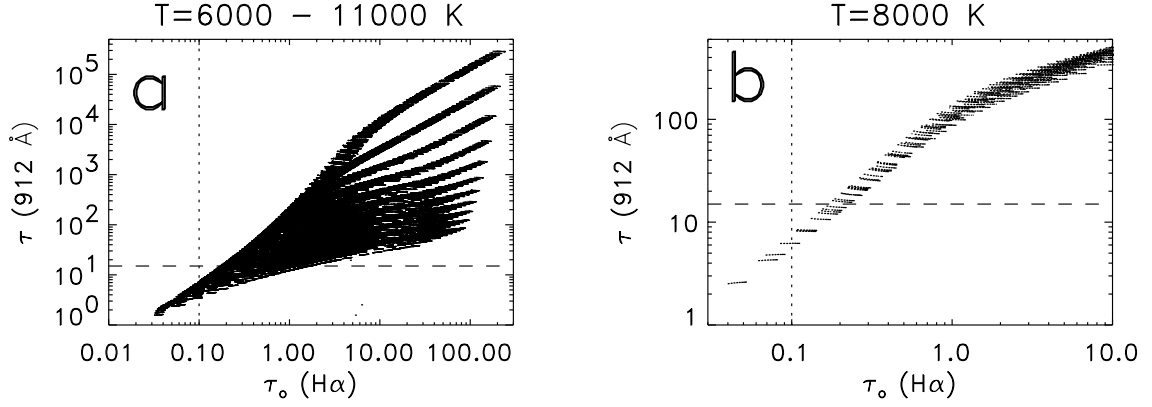


**Fig. 12.** **a)** Correlation between  $\tau_0(\text{H}\alpha)$  and  $\tau(912 \text{ \AA})$  for 11 temperatures (top curve: 6000 K, the step is 500 K). **b)** Correlation between  $\tau_0(\text{H}\alpha)$  and  $\tau(912 \text{ \AA})$  only for  $T = 8000 \text{ K}$ . For both figures the microturbulence variation is from 3 to  $10 \text{ km s}^{-1}$ . The dotted line represents the lower limit of optical thickness for which  $\text{H}\alpha$  filaments are detectable and the dashed line the upper limit for which the EUV absorption is not saturated.

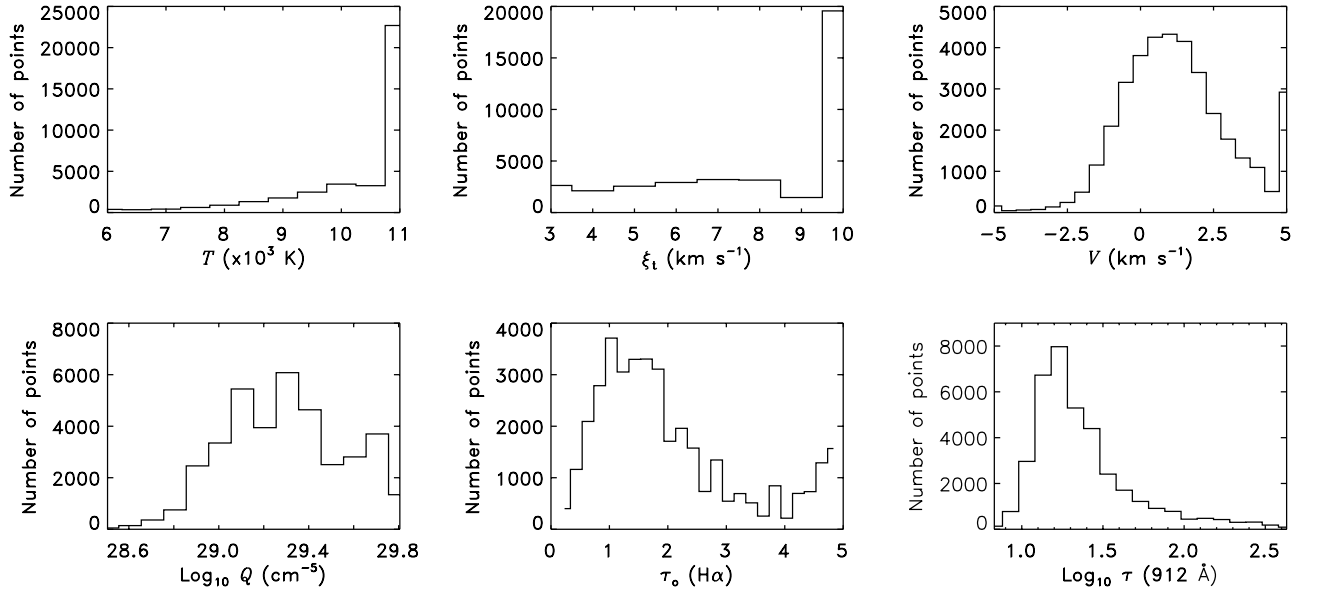


**Fig. 13.** The distributions of temperature  $T$ , microturbulence  $\xi_t$ , velocity  $V$ , emission measure  $Q$ ,  $\text{H}\alpha$  line-center optical depth  $\tau_0$  and Lyman continuum optical depth  $\tau(912 \text{ \AA})$  for the inversion of all filament profiles with a contrast (see text) lower than 0.96.

point of the observed filament. For the uniqueness of the solutions to the above fitting procedure we refer the reader to the paper by Molowny-Horas et al. (1999).

### 3.3.2. Theoretical opacity correlations

The optical thickness of the Lyman continuum  $\tau(912 \text{ \AA})$  for each of our grid models is calculated from the line-center optical thickness  $\tau_0$  of  $\text{H}\alpha$  using the relation

$$d\tau(912 \text{ \AA}) = \frac{\alpha_o(912) n_1}{\alpha_o(\text{H}\alpha) n_2} d\tau_0(\text{H}\alpha) \quad (3)$$

where  $n_1$  and  $n_2$  are, respectively, the first and second hydrogen level populations and  $\alpha_o(912)$  and  $\alpha_o(\text{H}\alpha)$  the absorption cross-sections for the Lyman continuum head and the  $\text{H}\alpha$  line center. The dependence on temperature comes partly from  $\alpha_o(\text{H}\alpha)$  which depends on the  $\text{H}\alpha$  Doppler width. The correlation between  $\tau(912 \text{ \AA})$  and  $\tau_0(\text{H}\alpha)$  for all the models of our grid,

shown in Fig. 12, suggests that as the temperature increases the ratio of the two aforementioned optical depths decreases. This is consistent with the analytical derivation of this ratio by Heinzel et al. (2001). We should note that the ratio of the two optical depths is very sensitive to the temperature, as Fig. 12 clearly demonstrates.

### 3.3.3. Results

For the grid-based inversion procedure we consider only those filament points which have a contrast profile relative to the background intensity ( $C_{\text{H}\alpha} + 1$ ) less than 0.96 (a total of 32564 filament profiles). This ensures that we exclude the filament borders and consider only profiles within its body. We use the same observed background profile and proportionality factor for the calibration (see Sect. 3.2) as for the constant source function inversion method. In Fig. 13 we present the histogram

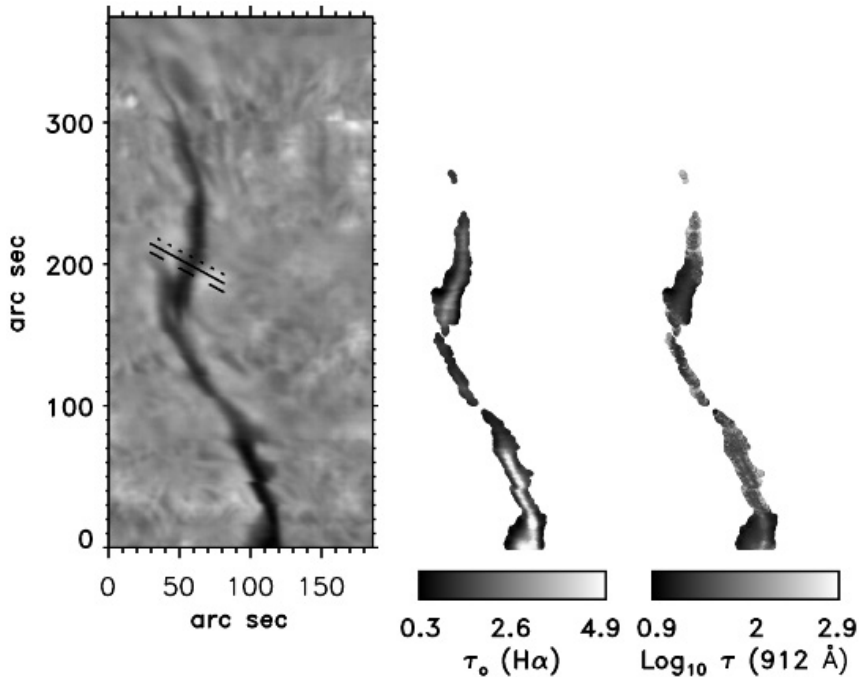


**Fig. 14.** *THEMIS*  $H\alpha$  line center image of the filament region and the inversion maps of the  $H\alpha$  line-center optical thickness and the corresponding Lyman continuum optical thickness. The thick lines (solid, dotted and dashed) on the  $H\alpha$  filament image show the positions of the three cuts of Fig. 15.

distributions of temperature  $T$ , microturbulence  $\xi_t$ , velocity  $V$ , emission measure  $Q$  (defined as  $N_e^2 Z$ ), line-center optical thickness  $\tau_0$  of  $H\alpha$  and optical thickness of the Lyman continuum  $\tau(912 \text{ \AA})$  for the inversion. The temperature and microturbulence distributions, which give an average temperature of 10 400 K and an average microturbulence of  $8.2 \text{ km s}^{-1}$ , show no other particular peak away from the borders of the grid as it has already been noticed and explained by Tziotziou et al. (2001). The velocity distribution shows a peak around  $1 \text{ km s}^{-1}$  and has an average value of  $1.5 \text{ km s}^{-1}$  while the emission measure distribution peaks around  $10^{29.2} \text{ cm}^{-5}$ . Finally, the  $H\alpha$  line-center optical thickness distribution is relatively broad with an average value of 2 and a peak around 1.5 and the Lyman continuum optical thickness has an average value of 40 and peaks around 18.

The Lyman continuum optical thickness is on average one order of magnitude higher than the equivalent  $H\alpha$  optical depth. However, this is a result of the high temperatures – close to 11 000 K – that the inversion gives, which as Fig. 12 demonstrates, show the lowest ratio between the two optical thicknesses. A cooler filament ( $T \sim 8000 \text{ K}$ ) would have a higher ratio ( $\sim 100$ ) between the Lyman continuum and  $H\alpha$  optical thickness (but see Sect. 4). We should bear in mind that as we have already mentioned the calculation of temperature is unreliable from  $H\alpha$  observations alone and the calculated temperature from the inversion seems to be far higher than the typical temperature for filaments (see Hvar reference atmosphere of quiescent prominences, Engvold et al. 1990). It is obvious that the calculated ratio from the inversion represents a minimum value. We further discuss this in the next section.

In Fig. 14 we present a *THEMIS*  $H\alpha$  line center image of the filament and the resulting maps from the inversion of the line-center  $H\alpha$  and Lyman continuum optical depths. Both maps suggest, as one would expect, that the filament is optically thicker in its center and the optical thickness decreases

as we move outwards. The inversion gives values for  $\tau(H\alpha)$  close to 0.3 near the borders of the map and since  $\tau(H\alpha)$  decreases from the center outwards, we can assume that outside the inverted filament  $\tau(H\alpha)$  is much lower than 0.3 resulting in a contrast intensity too low to be measurable and hence in an  $H\alpha$  filament channel which is less wide than the observed EUV filament.

In Fig. 15 we show the inversion values for the line-center  $H\alpha$  and Lyman continuum optical thickness along three  $50''$  cuts (see Fig. 14) which are  $4.4''$  apart and situated almost at the same position along the *SUMER* slit. Fig. 15b shows a region with  $\tau(912)$  between 0 and 10 but this is the region where  $H\alpha$  is optically thin and thus this determination by cloud-model inversion is not very good and we get very steep gradients compared to Fig. 9 (where  $\tau(912)$  comes from EUV absorption computation). On the other hand the EUV opacity for  $\tau(912) > 10$  cannot be computed from EUV absorption due to the complete absorption of the background radiation by the filament. But we can determine it from cloud-inversion methods where we get  $\tau(H\alpha)$  and convert it to  $\tau(912)$  using the curves of Fig. 12a. However since we use  $T = 11\,000 \text{ K}$  only the lowest curve applies and we get  $\tau$  up to 20 and not higher. A temperature of 8000 K would have lead to  $\tau(912) = 200$  due to the high sensitivity of the ratio of the optical thickness to the temperature (Fig. 12b). The two determinations of  $\tau(912)$  by cloud model and by EUV absorption are complementary.

A comparison of the results of the two different inversion methods presented so far shows that the distributions of the  $H\alpha$  optical thickness and the mean values of the respective distributions are different. This is associated with the range of Doppler widths for the two methods which is  $0.28$  to  $0.59 \text{ \AA}$  for the method with constant source function and  $0.23$  to  $0.37 \text{ \AA}$  for the grid method (the latter is directly calculated from the lower and upper limits of temperature and microturbulence taken into account for the inversion). Since the optical thickness increases

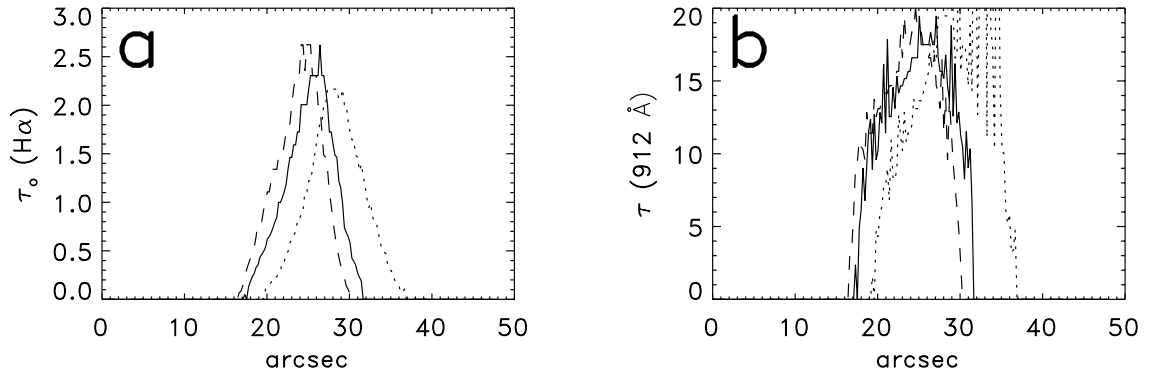


**Fig. 15.** a) The  $H\alpha$  line-center optical depth and b) the Lyman continuum optical depth along the three  $50''$  cuts shown at Fig. 14. The three cuts are situated almost at the same position along the *SUMER* slit.

with decreasing Doppler widths this would explain the higher optical thickness distribution for the grid method. We should remind the reader that the calculated optical thickness with the constant source function method represents, as we have already mentioned, a lower limit. The velocity distributions seem to be in good agreement as the scatter plot of the two calculated velocities shows in Fig. 16, with the velocities from the non-LTE grid calculations being on average  $1 \text{ km s}^{-1}$  higher. As we have already mentioned in Sect. 3.2, the used observed background is almost that of the quiet Sun. There is however a small difference in the wings of this profile with the quiet Sun profile from David (1961), which was used for the synthetic profile calculations. Our calculations show that this difference corresponds to a velocity of the order of  $1 \text{ km s}^{-1}$ . As a result the comparison of the observed profiles with the synthetic profiles will introduce this systematic velocity shift into the velocity of the grid method. This shift does not exist for the constant source function method since the method does not involve the comparison with a synthetic profile that has been calculated with the Quiet Sun background profile from David (1969). Our study confirms the results of Molowny-Horas et al. (1999) that even a cloud model with constant source function gives a rather accurate description of the velocity distribution within the filament. However, we should point out that the calculation of the velocity distribution with the non-LTE grid method, when the background is properly taken into account, is generally more accurate since the velocity is not only used in the optical thickness calculations but it also enters the calculations of the source function  $S$ . It is a well known property of cloud models that velocities derived from such inversion methods – like the ones used so far in our analysis – are always larger compared to Doppler shifts derived from line shifts from an average profile (see Fig. 1). Only for more optically thick structures both methods give the same results and hence in our case the correct velocity is that derived with our inversions.

#### 4. Non-LTE filament models based on *SUMER* spectra

We use the unique opportunity of having simultaneous spectra from *SUMER* (hydrogen Lyman lines plus the continuum) and from the *THEMIS* telescope in the  $H\alpha$  line to perform a

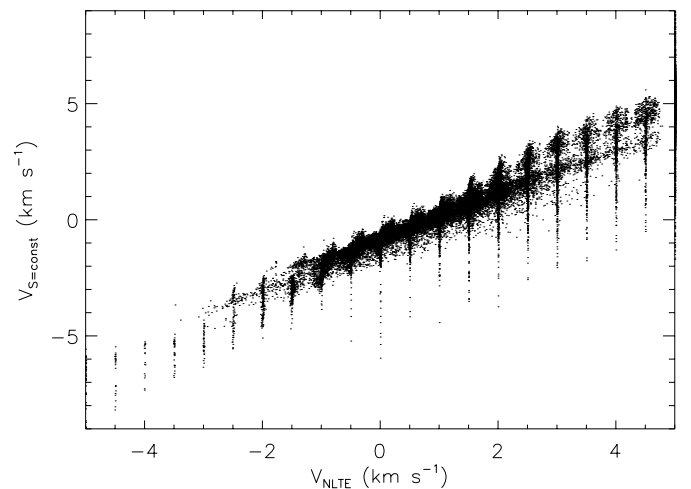


**Fig. 16.** Scatter plot between the calculated velocities from the constant source function method described in Sect. 3.2 and the non-LTE grid method described in Sect. 3.3. The concentration of the non-LTE velocities around the grid values is due to the parabolic interpolation method that follows the inversion in order to define more accurately the parameter.

multi-line non-LTE diagnostics of the filament under study. In Fig. 2 we have depicted the two locations where the *SUMER* slit intersects the filament at two different times of observation. We focus our attention on spectra taken at point A at 08:39 UT due to its proximity to the *THEMIS* observing time (see Fig. 5). Calibrated emission profiles of Lyman lines L5 to L11, together with the intensity of the Lyman continuum, are shown in Fig. 17 (thin line). They correspond to long exposure time spectra and the profiles are averaged over 5 pixels ( $5''$ ). To compute corresponding synthetic line and continuum intensities, we have used the same non-LTE code as described in Heinzel et al. (1997) and Schmieder et al. (1998). The filament is approximated by a 1D slab, parallel to the solar surface. Its lower boundary is placed at the height of 10 000 km and is irradiated by the underlying solar surface. We take this value because we do not know the bottom height of the  $H\alpha$  filament (in any case, this affects only the dilution factor which is not very sensitive to height). On the top, no radiation impacts on the filament from the corona (in hydrogen lines and continua). We solve the radiative-transfer and statistical-equilibrium equations for



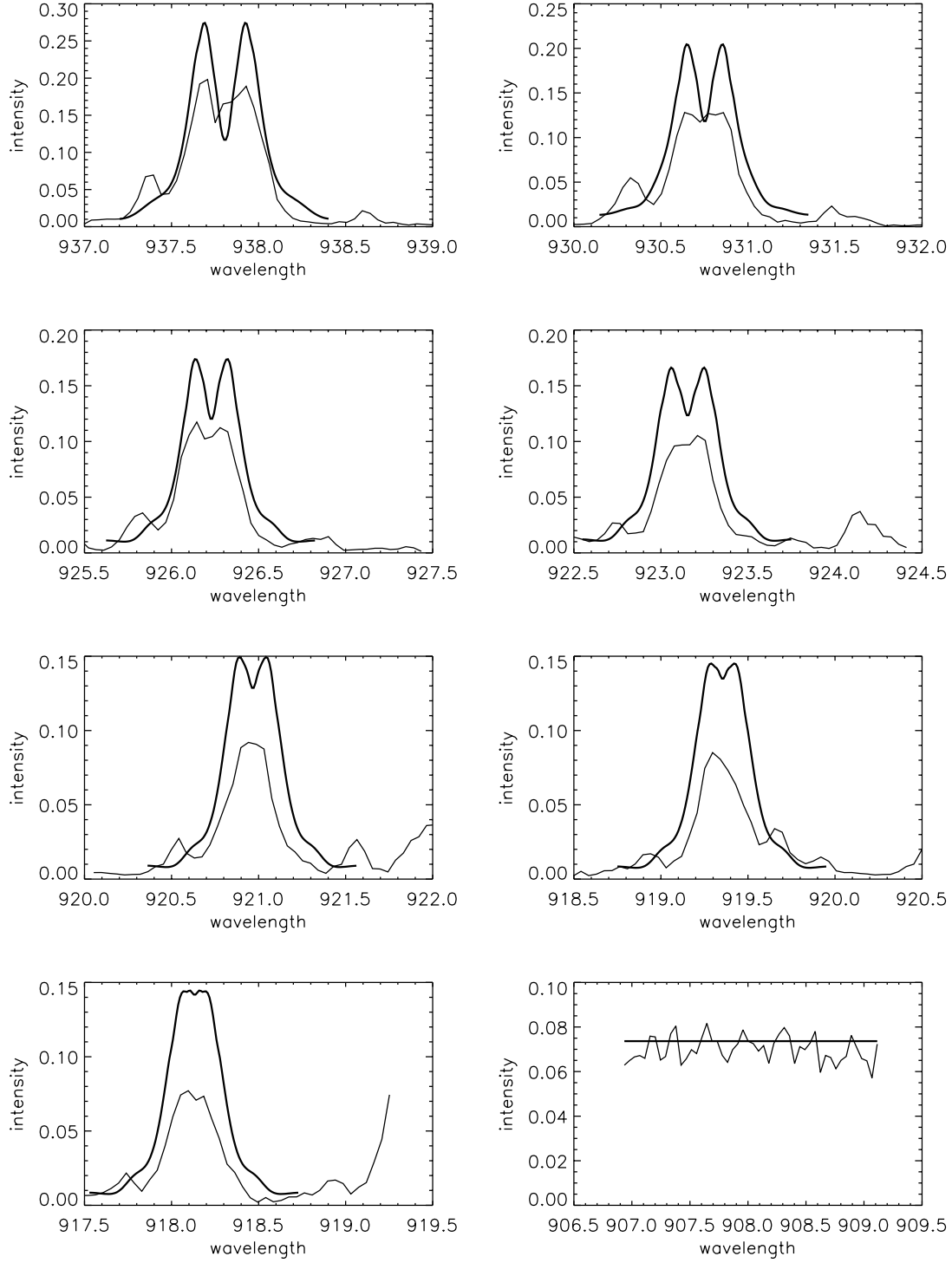


**Fig. 17.** Emission profiles of Lyman lines L5 to L11 and the Lyman continuum from calibrated *SUMER* observations (thin line) and from the non-LTE calculations described in Sect. 4.

a 5-level plus continuum hydrogen model in order to derive the electron-density structure (assuming an isobaric slab with the gas pressure as input parameter). In the next step we use a 12-level plus continuum model to obtain the synthetic spectra of the Lyman series and continuum, using the fixed electron density from previous step. In both steps we use the partial redistribution in  $L\alpha$  and  $L\beta$  lines as discussed in Heinzel et al. (1997). The 1D slab has a transition region between the

prominence and the corona (named PCTR) with prescribed temperature gradient, otherwise the Lyman line cores would be unrealistically deep as found in Schmieder et al. (1998) (e.g. using isothermal slabs).

After several trial-and-error simulations we have found an optimum model which approximately fits the *SUMER* spectra and also roughly satisfies the constraints imposed by the inversion of *THEMIS*  $H\alpha$  data. The latter are the line-center

$H\alpha$  optical thickness  $\tau_0(H\alpha) = 2.6$  and the emission measure  $Q = 3.7 \times 10^{29} \text{ cm}^{-5}$ . The parameters of the optimum model are: geometrical thickness  $Z = 5000 \text{ km}$ , central temperature  $T_c = 8000 \text{ K}$ , a PCTR layer of  $200 \text{ km}$  with a temperature rise to  $13\,000 \text{ K}$ , the gas pressure  $p = 0.08 \text{ dyn cm}^{-2}$ , the microturbulent velocity  $\xi_t = 5 \text{ km s}^{-1}$  and helium to hydrogen abundance ratio equal to  $0.1$ . Note several similarities of this model and fitted lines with those presented by Schmieder et al. (1998).

The resulting synthetic profiles are displayed in Fig. 17 (thick line). We see a general agreement between computed and observed intensities (with an accuracy of 30–40%, see Sect. 2.3), we also reproduce the trend of a gradual diminishing of the central reversal for higher members of the Lyman series. All profiles have been convolved with the corresponding *SUMER* instrumental profile. It is rather difficult, within this schematic 1D model, to fit simultaneously higher Lyman lines and the continuum: decreasing theoretical line intensities leads to a decrease of the Lyman continuum intensity. However, for the purposes of the present study, our current model seems to be satisfactory. It shows that the central temperature is around  $8000 \text{ K}$  and cannot be much higher, otherwise strong reversed profiles will appear in all lines and also the Lyman continuum will be too bright. Therefore, we cannot rely on the kinetic temperature derived from  $H\alpha$  inversions ( $11\,000 \text{ K}$ ). However, the  $H\alpha$  optical thickness  $\tau_0 = 3.2$  and the emission measure  $Q = 2.8 \times 10^{29} \text{ cm}^{-5}$ , derived from our best-fit non-LTE model are in good agreement with those obtained by the inversion of  $H\alpha$  profiles along the *SUMER* slit (see Fig. 15). The electron density is around  $2 \times 10^{10} \text{ cm}^{-3}$ .

We can immediately get from the best-fit model the value of the Lyman-continuum optical thickness  $\tau(912 \text{ \AA}) = 70$ . The determination of the  $H\alpha$  optical thickness (previous sections) gives  $\tau_0 = 3.2$  for  $H\alpha$ . The corresponding  $\tau(912 \text{ \AA})$  is around 200 according to the graph of Fig. 12b for a temperature  $T = 8000 \text{ K}$ . Comparing these two values, we find that the value determined from Lyman lines is too low. However, one has to keep in mind that the grid used to construct Fig. 12 was actually computed with the complete redistribution in Lyman lines, which is an excellent approximation if the electron density is given and if one is interested only in subordinate lines (Heinzel 1995). If we use complete redistribution in the second step of non-LTE computations, we arrive at a value of 200 which is compatible with Fig. 12. So we can make an important conclusion that the partial redistribution *lowers* the ratio of Lyman-continuum to  $H\alpha$  opacity. Second, the observed as well as computed Lyman-continuum intensity at  $912 \text{ \AA}$  is lower as compared to the quiet Sun and thus we can see a dark filament at this wavelength. However, the total absorption of the background quiet-Sun radiation is significantly compensated by the filament radiation. This is not the case of the EUV absorption model. The actual observed contrast in the Lyman continuum is shown in Fig. 6 and we see that the low intensity value channel corresponds to the EUV filament, the intensity bump at pixel 20 corresponds to the quiet-Sun crossed by the *SUMER* slit. The darkness of the filament in Lyman lines and continuum is caused by the fact that the corresponding source function at

optical depth around one is lower than the background intensity, while the background radiation is totally absorbed.

## 5. Discussion and conclusions

A very detailed analysis of a quiescent filament observed during a MEDOC campaign on May 5, 2001 was performed. Multi wavelength data were obtained simultaneously with *SOHO/CDS - SUMER* and *THEMIS*.

A wide EUV filament has been identified as a dark area observed in the *CDS* images. The EUV filament width reaches  $100''$  when it shows long lateral extensions on both sides of its axis. The width of the associated  $H\alpha$  filament is only  $10''$  or  $20''$  depending on the position along the filament and the presence of footpoints. The EUV lateral extensions are not necessarily related to the  $H\alpha$  footpoints.

This study confirms the existence of cool material in the vicinity of the  $H\alpha$  filament (Heinzel et al. 2001). We computed the optical thickness at the head of Lyman continuum of this plasma at  $912 \text{ \AA}$  by using different methods taking the opportunity of coordinated observations.

We construct a model which could explain the large depression observed in *CDS* rasters taking into account the scale-height of the different lines. A consistent study is performed by considering an extended cloud of cool and low density gas located in the filament channel. The reduced emission of the transition-region line (e.g.  $O\text{ v}$ ) is due to the absorption by the hydrogen Lyman continuum. The ratio between the intensities of the EUV filament and the surrounding atmosphere leads to the determination of  $\tau(912)$  in the regions where  $\tau(912)$  is  $< 10$ – $15$ . In the regions of higher  $\tau(912)$  the opacities of  $H\alpha$  and of the Lyman continuum are determined by a sophisticated inversion method using a grid of models (81160 models) computed for a large parameter space with a multi-level non-LTE radiative transfer code (Tziotziou et al. 2001). This grid allows us to compute the relationship that exists between  $\tau(H\alpha)$  and  $\tau(912)$  as a function of temperature. For a temperature of  $8000 \text{ K}$ , an optical thickness of Lyman continuum of 15 would correspond to an optical thickness of  $H\alpha$  around  $0.1$ , that is a lower limit where  $H\alpha$  filament is detectable and explains why we do not see this large extended cloud in  $H\alpha$  observations.

In the  $H\alpha$  filament, the grid inversion method gives directly the values of  $H\alpha$  and Lyman continuum optical thicknesses. We found a maximum value of  $\tau(H\alpha)$  of 3 and of  $\tau(912)$  around 20 at a temperature of  $11\,000 \text{ K}$ . This  $\tau(H\alpha)$  value would correspond to a  $\tau(912)$  of 200 in a temperature of  $8000 \text{ K}$ . Unfortunately, the inversion method does not allow us to get a precise value of the temperature.

To determine the temperature with accuracy we have analyzed the Lyman line profiles observed by *SUMER*. Using the observations of the Lyman series and continuum, with non-LTE modeling we have successfully obtained, for the few points along the *SUMER* slit that cut the filament, good diagnostics of filament plasma conditions (temperature of  $8000 \text{ K}$  for a filament with a PCTR layer up to  $13\,000 \text{ K}$ , a geometrical thickness of  $5000 \text{ km}$ , a microturbulence of  $5 \text{ km s}^{-1}$  and a gas pressure of  $0.08 \text{ dyn cm}^{-2}$ ). The obtained  $H\alpha$

optical thickness and the emission measure are in reasonable agreement with the values determined from the previous  $H\alpha$  inversion, while the Lyman continuum opacity in the filament is about 80. This lower value is explained by the use of partial-redistribution in the non-LTE modeling.

In conclusion we have derived the  $\tau(912)$  distribution by different methods and approaches (0–10 in the EUV filament and 10–200 in the  $H\alpha$  filament). The uncertainty of the different methods has been included in these distributions. It can reach a factor of 2 due to the uncertain background which changes between 500 and 1000 for O v. All the aforementioned approaches seem to confirm the importance of the Lyman-continuum absorption and volume-blocking model. The presence of cool material in the wide EUV filament can be further supported by recent filament modeling based on the presence of dips in thin twisted flux tubes (Anzer & Heinzel 2003) or in a global 3D configurations (Aulanier & Démoulin 1998; Aulanier & Schmieder 2002). These authors predict a larger mass content for the filament body which will contribute to a possible CME mass load.

However, many questions still remain to be answered, in particular:

- Is the cool material located in lateral extensions of EUV filaments lying at low heights and will it not participate in filament eruption as the magnetic model of Aulanier & Schmieder (2002) suggests? A center to limb filament study using EUV lines and  $H\alpha$  would be a good test of the model.
- How does the EUV filament evolve during an eruption? Is it still visible? Is the cool material heated, making a halo around the prominence as suggested by Engvold et al. (2001), or is this halo just due to diffuse emission (Heinzel et al. 2001)?
- Is the assumption of the non-existence of a void completely justified? Coordinated observations in radio wavelengths should be very useful and observations of filaments close to the limb should allow us to disentangle the two phenomena: absorption and lack of coronal emission.

**Acknowledgements.** *THEMIS* is a French-Italian telescope operated on the island of Tenerife by CNRS-CNR in the Spanish Observatorio del Teide of the Instituto de Astrofísica de Canarias. SoHO is a project of international cooperation between ESA and NASA. P.H. thanks A. Gabriel (*CDS* planner), W. Curdt and the MEDOC staff for their help during the campaign, and B.S. acknowledges the support of the *THEMIS* staff and of J.-M. Malherbe during her observations. We are indebted to P. Mein for all his help in data reduction and comments on the paper. We also thank P. Rudawy for his help and comments concerning the data calibration. U. Anzer contributed considerably to development of a consistent absorption and blocking model. Finally, we would like to thank O. Engvold, A. Fludra, W. Thompson and J.E. Wiik for discussions and comments and the referee for the very constructive suggestions which helped us to extensively improve the whole paper. K.T. thanks CNRS for travel support and the Astronomical Institute at Ondřejov for hospitality.

P.H. was supported by CNRS and by grants S-1003006 and A3003203 of the Academy of Sciences of the Czech Republic. K.T. and B.S. acknowledge support through an EC-TMR grant to the European Solar Magnetometry Network.

## References

- Anzer, U., & Heinzel, P. 2003, *A&A*, submitted
- Aulanier, G., & Démoulin, P. 1998, *A&A*, 329, 1125
- Aulanier, G., & Schmieder, B. 2002, *A&A*, 386, 1106
- Brooks, D. H., Fishbacher, G. A., Harrison, R. A., Innes, D. E. et al. 1999, *A&A*, 347, 277
- Chiuderi Drago, F., Alissandrakis, C. E., Bastian, T., Bocchialini, K., & Harrison, R. 2001, *Sol. Phys.*, 199, 115
- David, K. H. 1961, *Z. Astrophys.*, 53, 37
- Engvold, O., Hirayama, T., Leroy, J. L., Priest, E. R., & Tandberg-Hanssen, E. 1990, in *Dynamics of Quiescent Prominences*, IAU Colloq. 117, ed. V. Ruždjak, & E. Tandberg-Hanssen (Springer-Verlag), *Lect. Notes Phys.*, 363, 294
- Engvold, O., Jakobsson, H., Tandberg-Hanssen, E., Gurman, J. B., & Moses, D. 2001, *Sol. Phys.*, 202, 293
- Fludra, A., del Zanna, G., Alexander, D., & Bromage, B. J. I. 1999, *J. Geophys. Res.*, 104, 9709
- Fludra, A., Ireland, J., del Zanna, G., & Thompson, W. T. 2002, *Adv. Space Res.*, 29, 361
- Harrison, R. A., Sawyer, C., Carter, M. K., et al. 1995, *Sol. Phys.*, 162, 233
- Heinzel, P. 1995, *A&A*, 299, 563
- Heinzel, P., Schmieder, B., & Vial, J. C. 1997, *SOHO 5 Workshop*, Oslo, ESA SP-404, p. 427
- Heinzel, P., Mein, N., & Mein, P. 1999, *A&A*, 346, 322
- Heinzel, P., Schmieder, B., & Tziotziou, K. 2001, *ApJ*, 561, L223
- Heinzel, P., Anzer, U., & Schmieder, B. 2003, in preparation
- Kucera, T. A., Andretta, V., & Poland, A. I. 1998, *Sol. Phys.*, 183, 107
- Martin, S. F. 1998, *Sol. Phys.*, 182, 107
- Mein, N., Mein, P., Heinzel, P., et al. 1996, *A&A*, 309, 275
- Mein, N., Schmieder, B., DeLuca, E. E., et al. 2001, *ApJ*, 556, 438
- Mein, P., Mein, N., & Malherbe, J.-M. 1985, *MPA/LPARL Workshop* in Munich, p. 303
- Mein, P. 1991, *A&A*, 248, 669
- Mein, P. 2002, *A&A*, 381, 271
- Mihalas, D. 1978, *Stellar Atmospheres*, 2nd edn. (San Francisco: W.H. Freeman)
- Molowny-Horas, R., Heinzel, P., Mein, P., & Mein, N. 1999, *A&A*, 345, 618
- Penn, M. 2000, *Sol. Phys.*, 197, 313
- Plunkett, S. P., Vourlidas, A., Simberová, S., et al. 2000, *Sol. Phys.*, 194, 371
- Schmahl, E. J., & Orrall, F. Q. 1979, *ApJ*, 231, L41
- Schmieder, B., Heinzel, P., Kucera, T., & Vial, J. C. 1998, *Sol. Phys.*, 181, 309
- Schmieder, B., Tziotziou, K., Heinzel, P., Malherbe, J.-M., & Curdt, W. 2003, *Nuevo Cimento*, in press
- Schüle, U., Hollandt, J., Pauluhn, A., & Wilhelm, K. 2000, *ESA*, SP-463, 427
- Sterling, A. C., Pike, C. D., Mason, H. E., Watanabe, T., & Antiochos, S. K. 1999, *ApJ*, 524, 1096
- Tziotziou, K., Heinzel, P., Mein, P., & Mein, N. 2001, *A&A*, 366, 686
- Wilhelm, K., Curdt, W., Marsch, E., et al. 1995, *Sol. Phys.*, 162, 189
- Wilhelm, K., Lemaire, P., Curdt, W., et al. 1997, *Sol. Phys.*, 170, 75